

The 10 Meter South Pole Telescope

J. E. Carlstrom,^{1,2,3,4} P. A. R. Ade,⁵ K. A. Aird,⁶ B. A. Benson,⁷ L. E. Bleem,^{1,4} S. Busetti,⁸ C. L. Chang,^{1,4} E. Chauvin,⁸ H.-M. Cho,⁹ T. M. Crawford,^{1,2} A. T. Crites,^{1,2} M. A. Dobbs,¹⁰ N. W. Halverson,¹¹ S. Heimsath,⁶ W. L. Holzapfel,⁷ J. D. Hrubes,⁶ M. Joy,¹² R. Keisler,^{1,3} T. M. Lanting,¹⁰ A. T. Lee,⁷ E. M. Leitch,^{1,2} J. Leong,¹³ W. Lu,¹³ M. Lueker,⁷ D. Luong-Van,^{1,2} J. J. McMahon,^{1,4} J. Mehl,⁷ S. S. Meyer,^{1,2,3,4} J. J. Mohr,¹⁴ T. E. Montroy,¹³ S. Padin,^{1,2} T. Plagge,⁷ C. Pryke,^{1,2,4} J. E. Ruhl,¹³ K. K. Schaffer,^{1,4} D. Schwan,⁷ E. Shirokoff,⁷ H. G. Spieler,¹⁵ Z. Staniszewski,¹³ A. A. Stark,¹⁶ C. Tucker,⁵ K. Vanderlinde,^{1,2} J. D. Vieira^{1,3} and R. Williamson^{1,2}

jc@kicp.uchicago.edu

¹Kavli Institute for Cosmological Physics, University of Chicago, 5640 South Ellis Avenue, Chicago, IL 60637

²Department of Astronomy and Astrophysics, University of Chicago, 5640 South Ellis Avenue, Chicago, IL 60637

³Department of Physics, University of Chicago, 5640 South Ellis Avenue, Chicago, IL 60637

⁴Enrico Fermi Institute, University of Chicago, 5640 South Ellis Avenue, Chicago, IL 60637

⁵Department of Physics and Astronomy, Cardiff University, CF24 3YB, UK

⁶University of Chicago, 5640 South Ellis Avenue, Chicago, IL 60637

⁷Department of Physics, University of California, Berkeley, CA 94720

⁸General Dynamics Satcom Technologies, 2205 Fortune Drive, San Jose CA 95131

⁹National Institute of Standards and Technology, Boulder, CO 80305

¹⁰Department of Physics, McGill University, 3600 Rue University, Montreal, Quebec H3A 2T8, Canada

¹¹Department of Astrophysical and Planetary Sciences and Department of Physics, University of Colorado, Boulder, CO 80309

¹²Department of Space Science, VP62, NASA Marshall Space Flight Center, Huntsville, AL 35812

¹³Department of Physics, Case Western Reserve University, Cleveland, OH 44106

¹⁴Department of Astronomy and Department of Physics, University of Illinois, 1002 West Green Street, Urbana, IL 61801

¹⁵Physics Division, Lawrence Berkeley Laboratory, Berkeley, CA 94720

¹⁶Harvard-Smithsonian Center for Astrophysics, 60 Garden Street, Cambridge, MA 02138

Received _____; accepted _____

ABSTRACT

The South Pole Telescope (SPT) is a 10 m diameter, wide-field, offset Gregorian telescope with a 966-pixel, multi-color, millimeter-wave, bolometer camera. It is located at the Amundsen-Scott South Pole station in Antarctica. The design of the SPT emphasizes careful control of spillover and scattering, to minimize noise and false signals due to ground pickup. The key initial project is a large-area survey at wavelengths of 3, 2 and 1.3 mm, to detect clusters of galaxies via the Sunyaev-Zeldovich effect and to measure the small-scale angular power spectrum of the cosmic microwave background (CMB). The data will be used to characterize the primordial matter power spectrum and to place constraints on the equation of state of dark energy. A second-generation camera will measure the polarization of the CMB, potentially leading to constraints on the neutrino mass and the energy scale of inflation.

1. Introduction

Observations of the cosmic microwave background (CMB) radiation have enormous power to address fundamental questions in cosmology. Primary temperature and polarization anisotropies in the CMB provide a unique view of the primordial plasma, while secondary anisotropies yield information about the structures that have formed in the universe (e.g., Hu & Dodelson 2002). The cosmological information encoded in the medium- and large-scale CMB temperature anisotropy, measured with exquisite precision by the *WMAP* instrument (Nolta et al. 2009), provides some of the most important evidence in support of our current cosmological model (Dunkley et al. 2009). This model has been further strengthened by the detection and measurement of so-called “E-mode” CMB

polarization anisotropy (e.g., Kovac et al. 2002; Page et al. 2007). The next frontiers in CMB anisotropy measurement are the small-scale secondary anisotropies and the “B-mode” polarization signature. Measuring this next generation of signals is the main scientific motivation for the South Pole Telescope (SPT).

The most significant source of small-scale secondary CMB anisotropy is expected to be the Sunyaev-Zeldovich (SZ) effect, in which CMB photons are scattered by hot electrons in the deep potential wells of massive clusters of galaxies (Sunyaev & Zel’dovich 1972). The SZ effect is a potentially powerful tool for finding clusters at high redshift (e.g., Carlstrom et al. 2002). A sufficiently sensitive SZ cluster survey can produce a large, nearly mass-limited sample of clusters. Follow-up measurements of photometric redshifts will then allow determination of the cluster abundance as a function of redshift. This is a sensitive probe of structure formation, capable of providing strong constraints on the amplitude of density fluctuations and on the density and equation of state of dark energy (Holder et al. 2001). Additionally, a measurement of the angular power spectrum of this signal will yield constraints on cosmological parameters that are complementary to those from a cluster survey (Komatsu & Seljak 2002).

Measurements of the B-mode polarization anisotropy of the CMB probe the gravitational wave background generated during inflation (Polnarev 1985; Crittenden et al. 1993; Seljak & Zaldarriaga 1997; Seljak 1997). This is a unique opportunity to probe physics at the earliest epochs and highest energies, but it requires unprecedented raw sensitivity and exquisite control of systematics. The situation is complicated further because gravitational lensing of the E-mode CMB polarization by large-scale structure also generates B-mode polarization. Unraveling the signals will require measurements over a wide range of angular scales (Okamoto & Hu 2003; Knox & Song 2002). The lensing polarization signal is interesting in its own right. It is another probe of the growth of

large-scale structure, so it can also provide constraints on the equation of state of dark energy, curvature and the neutrino masses (e.g., Tegmark 2005).

The measurements of the CMB necessary to achieve these science goals involve imaging large areas of sky with high sensitivity at millimeter wavelengths. The best bolometer detectors in this band are already close to sky-noise limited (Richards 1994; Holland et al. 2002). Therefore, the SPT aims to improve sensitivity by increasing the number of background-limited detectors, observing at the best site, and minimizing systematic errors. As discussed in Ruhl et al. (2004), the key performance features of the SPT are:

(1) ~ 1 arcmin beamwidth, to resolve the SZ effect from galaxy clusters. This requires an 8 m diameter or larger telescope at $\lambda = 2$ mm. The SPT has a 10 m primary with $20 \mu\text{m}$ rms surface error to facilitate future submillimeter observations. This level of angular resolution will also enable precise measurements of the B-mode polarization from gravitational lensing.

(2) Low scattering, to reduce detector loading and reduce potential systematic errors such as scan-synchronous offsets due to ground pick-up. This leads to an offset optical design with smooth mirrors to reduce scattering and ground shields to control spillover. The secondary mirror is cooled to ~ 10 K and surrounded by cooled absorbing baffles to limit scattered light and loading on the detectors.

(3) Unprecedented raw sensitivity, so we can quickly map large areas of sky to useful depths. An SZ survey must cover a large area of the sky to yield enough clusters to set useful constraints on dark energy—and the amplitude of the SZ effect from massive galaxy clusters is typically tens to hundreds of μK —while a CMB polarimeter must measure hundreds of square degrees of sky to μK noise levels to enable a measurement of the inflationary B-mode signal. This sensitivity requirement is met by a telescope with a wide field of view, filled with background-limited detectors.

(4) An excellent site for millimeter observing, in order that the survey sensitivity not be limited by atmospheric opacity or sky noise.

The current SPT camera has a 966-pixel, temperature-sensitive bolometer array receiver operating simultaneously in the 3, 2 and 1.3 mm atmospheric windows. This provides spectral discrimination against galactic foregrounds and radio and infrared extragalactic sources, and allows us to separate CMB and SZ signals. The camera uses transition edge sensor (TES) bolometer detectors with a noise equivalent temperature (NET) of $\sim 450 \mu\text{K}\sqrt{\text{s}}$ (in CMB temperature units) at $\lambda = 2$ mm. It is located at the Amundsen-Scott South Pole station, which is one of the best millimeter and submillimeter wave sites on Earth. The next camera on the SPT will be a multi-color polarimeter with similar, but even greater, raw sensitivity.

In Section 2 of this paper, we review the South Pole site. Sections 3 and 4 describe the design and performance of the optics and telescope, respectively. Section 5 contains an overview of the receiver. In Section 6 we describe our observing strategy. Conclusions are presented in Section 7.

2. Site

The South Pole is a high, dry site with exceptional atmospheric transparency and stability at millimeter and submillimeter wavelengths. In winter, the median precipitable water vapor is ~ 0.25 mm (Chamberlin 2001). The median brightness fluctuation power at $\lambda = 2$ mm is $\sim 31 \text{ mK}^2 \text{ rad}^{-5/3}$ in CMB temperature units (Bussmann et al. 2005). This is at least an order of magnitude better than other established terrestrial sites (Bussmann et al. 2005; Sayers et al. 2010). Temperatures can fall to -82 C in winter, which places severe constraints on the design of exposed components, but weather conditions are

otherwise fairly benign. The average pressure altitude in winter is 3300 m (cf. 2800 m physical altitude). Light ($\sim 5 \text{ m s}^{-1}$) katabatic winds blow from the East Antarctic Plateau most of the time (Schwerdtfeger 1984), and high winds are rare. The peak recorded wind speed is only 24 m s^{-1} . Snow accumulation is $\sim 150 \text{ mm yr}^{-1}$, but local drifting around surface structures is a problem, so most buildings are elevated. The ice pack is over 2 km thick and it moves $\sim 10 \text{ m yr}^{-1}$. Transport to the South Pole is via LC130 aircraft, which can carry 11,500 kg of cargo. Access is only possible between about 1st November and 14th February of each year. Air transportation and the short annual construction season are unique and challenging constraints to fielding instruments at the South Pole.

3. Optics

3.1. Optical design

The SPT (see Figure 1) is an offset classical Gregorian design. We chose this because: (1) the unblocked aperture minimizes noise and ground pickup, which is a serious problem for observations of faint, low-contrast emission such as the CMB; (2) a Gregorian configuration provides an image of the primary for a chopper or Lyot stop for future receivers; (3) the secondary in a Gregorian design is concave, which makes testing of the mirror easier; and (4) the paraboloidal primary of the classical form allows us to change the focal length of the secondary for future receivers. An aplanatic design offers a wider field of view (Hanany & Marrone 2002) but the focal length of the secondary cannot be changed much and the focal surface is more curved. The optical configuration of the SPT is unusually simple because the detectors are at the Gregory focus (see Figure 2 and Padin et al. (2008)). There are just 2 mirrors (primary and secondary) and a lens (to make the final focus telecentric and improve the illumination of the secondary). This scheme gives low loss, scattering and instrumental polarization, and makes alignment easy. The field of

view is roughly λ (mm) \times 0.7 degrees and is limited mainly by coma.

The primary has a 10 m diameter aperture with a focal length of 7 m. Prime focus is 300 mm below the bottom of the primary. This arrangement gives a reasonable compromise between aberrations, ease of manufacture, and the size of the secondary support structure. For more detailed parameters of the telescope optics, see Figure 2 and Table 1 of Padin et al. (2008).

Millimeter-wave telescopes usually have a chopping mirror that quickly scans or switches the beam to “freeze” atmospheric and gain fluctuations. A chopping secondary is sometimes used, but telescopes with a wide field of view usually have a flat chopping mirror at an image of the primary. The image of the primary just after a Gregorian secondary is a common choice. Wide field designs favor a fast secondary, to keep the size of the focal plane reasonable, but this gives a poor image of the primary and increases chop-synchronous offsets. For the SPT, we decided to abandon a chopper in favor of rapidly scanning the entire telescope. This works for the low-impedance TES bolometers and frequency domain readout in our receiver, but could be a problem for semiconductor bolometers, which are typically sensitive to vibration from the telescope drives. Avoiding a chopper was an important choice because it allowed us to make the Gregory focus fast enough to feed the detectors directly.

The SPT receiver has wafers of detectors mounted behind a close-packed array of smooth-wall, conical feedhorns. The spacing between horns is 4.8 mm, which gives reasonable separation between the 4 mm diameter pixels on the detector wafers and provides space for the readout wiring. For optimum coupling to a point source, the horn aperture diameter should be $2F\lambda$, where F is the final focal ratio (Griffin et al. 2002). For $\lambda = 2$ mm the $F1.3$ telescope optics are well matched to the horn apertures. The fast final focus moves the receiver close to the secondary, which increases the mass of the secondary

support structure. In addition, the small secondary magnification means the mirror must be tilted through a large angle to compensate aberrations (Dragone 1982). This requires that the receiver be located close to the beam from the primary. The receiver-to-beam clearance is a fairly severe constraint in the SPT design, but it is difficult to avoid without adding mirrors.

To control the illumination pattern of the primary while keeping loading low, the optical system must include a cold stop. The SPT optical design does not have a good image of the primary for a stop, so we moved the exit pupil to the secondary and surrounded the mirror with cold absorber. The absorber extends from the secondary to prime focus, and also into the receiver, so it functions both as the stop and as a shield around the beam. In this scheme, the obvious place for a cryostat window is near prime focus, where the beam is small. The large cold stop at the secondary does require additional cryogenics, and the primary must be a little larger because it is no longer the entrance pupil. The key advantage is good control of spillover because the entire beam from prime focus to the detectors is contained inside a cold, absorbing box.

With the exit pupil at the secondary, there is a trade-off between the size of the secondary and the size of the primary (Wilson 1996). A smaller secondary, and hence smaller receiver-to-secondary spacing, results in a larger shift of the illumination on the primary with field angle, so the primary must be made larger. This is expensive and it pushes the design towards a larger secondary. For the SPT, we chose a 1 m secondary, for which standard machining techniques can achieve $\sim 10 \mu\text{m}$ rms surface error. The primary must then be 1 m oversize, which fits with our 10 m aperture and our requirement for a 1 arcmin beam to resolve the SZ effect from clusters of galaxies at $\lambda = 2 \text{ mm}$.

The focal plane of a Gregorian telescope is curved, so we added a lens just in front of the detectors to make the final focus telecentric. This lens reduces the final focal length,

allowing us to use a slightly higher secondary magnification, which increases the clearance between the receiver and the beam. We optimized the lens to center the illumination pattern on the secondary for all detectors, which pushes the lens to a meniscus shape. At $\lambda = 2$ mm, the spillover on the stop is $20 \pm 0.5\%$, where the range indicates the variation in spillover across the detector array. The lens is made of high density polyethylene (HDPE) and is thermally linked to the 4 K cold head inside the receiver cryostat. The shape of the lens design accounted for a uniform 1.9% contraction of the HDPE as it cools to its operating temperature, which was measured in the lab to be 6-7 K. The surfaces of the lens are machined with circumferential triangular grooves to minimize reflections. These grooves are 0.56 mm wide and 0.64 mm deep, which is approximately a quarter wavelength for our $\lambda = 2$ mm detectors. These groove dimensions were optimized so that the calculated transmission was $> 98\%$ across each three of the observing bands.

3.2. Secondary and cold stop

The SPT cryostat has two independent sections that share the same vacuum space (see Figure 3). The optics cryostat contains the secondary mirror, most of the cold stop, and the window and associated heat-blocking filters. The receiver cryostat contains the lens, the band-defining filters and the detectors. Each cryostat has its own refrigerator system. This arrangement allows us to test the receiver without the optics cryostat and to change receivers without disrupting the secondary. The secondary and cold stop are supported by a truss that attaches to the receiver mounting flange on the optics cryostat. The detectors are attached to the other side of that flange via a cone and truss. The separation between the secondary and the detectors is fixed, but the cryostat assembly is mounted on an optical bench that can be moved ± 25 mm in any direction to maintain alignment with the primary (see Figure 4). This allows us to compensate gravitational flexure of the secondary support

structure and changes in the focal length of the primary with elevation (which are both a few mm over the full elevation range). The optical bench actuators have a maximum speed of 25 mm min^{-1} , so they can only follow slow changes.

The secondary is a lightweighted (20 kg) aluminum 7075-T6 mirror, 1 m in diameter \times 50 mm thick. It is attached at 3 points to a triangular back plate, which is in turn supported by a truss made of 20 mm diameter \times 1 mm wall stainless steel tubes. The truss rods have preloaded ball joint ends that allow some movement during cooling. The secondary surface profile error was initially $11 \text{ }\mu\text{m rms}$ at room temperature (measured using holography at 89 GHz), but this increased to $50 \text{ }\mu\text{m rms}$ when the mirror was cooled. It is now $23 \text{ }\mu\text{m rms}$ at room temperature. Stress inside the mirror is likely responsible for these changes. We did stress relieve the blank by cooling it to 77 K and then slowly warming to room temperature, 3 times, before the final cut. However, the first thermal cycles of the finished mirror were done in a mount that had no compliance between the mirror and its back plate. We will probably replace the secondary and improve its mount in the future.

The cold stop is microwave absorber (flexible foam sheet HR-10¹) cooled to 10 K. With 20% spillover, this contributes just a few K to detector background loading. The absorber is glued to the inside of a shroud made of annealed, i.e., high thermal conductivity, aluminum 1100. This is surrounded by a radiation shield made of the same material. Both the shroud and the shield are covered with 9 layers of superinsulation (NRC-2-Cryolam²) to reduce the radiation load. The secondary end of the 20 kg stop and shield assembly is attached to the mirror back plate. The other end is attached to the receiver mounting flange with an axial flexure. The flexure reduces the torque on the mirror support and allows the end of the stop and shield to move $\sim 3 \text{ mm}$ on cooling.

¹Emerson & Cuming, Billerica MA 01821

²Metallized Products Inc., Winchester MA 01890

Metal-mesh, heat-blocking filters (Tucker & Ade 2006) are attached to the stop shroud and radiation shield just behind the 100 mm thick expanded polypropylene foam (Zotefoam PPA30³) cryostat window. The loss through the window has been measured to be less than 0.5% at 2.1 mm. The stop assembly is cooled by a pulse tube refrigerator (Cryomech Inc., model PT410⁴) with a capacity of 10 W at 10 K and 80 W at 70 K. The stop cools to 10 K, with < 1 K gradient along its length, and the shield cools to 70 K at the heat-blocking filters and 60 K at the refrigerator end. Cooling time for the optics cryostat is 3 days.

Changes in the temperature of the cold stop are coupled to the detectors through the spillover from the feedhorns and this raises two concerns:

(1) Systematic signals due to temperature fluctuations from the pulse tube refrigerator. This turns out to be a small effect because the fluctuations are strongly attenuated by the low-pass filter formed by the thermal resistance of the various heat straps and the heat capacity of the stop shroud and secondary. A thermometer on the stop shroud shows $< 1 \mu\text{K}$ rms fluctuations at the 1.4 Hz pulse tube frequency. In addition, the pulse tube frequency is very stable in time and can be notched in the incoming data with negligible loss of information.

(2) Scan-synchronous offsets or systematic signals noise due to changes in loading on the cold stop from the cryostat window. The cold absorber has very low thermal conductivity, so changes in loading at the mW level could cause mK amplitude systematic signals in the detectors. This is addressed in the SPT design through careful filtering, which reduces the calculated heat load on the stop to ~ 20 mW. In addition, the Zotefoam cryostat window is opaque to IR radiation ensuring that the power reaching the stop is not significantly

³Zotefoams PLC, Croydon CR9 3AL UK

⁴Cryomech Inc., Syracuse NY 13211

modulated by the radiation coming through the cryostat window.

Mechanical stability of the stop is also a concern because any movement of the beam on the stop, filters, or window could change the spillover and generate scan-synchronous offsets. This signal is calculated to be $\sim 10 \text{ mK mm}^{-1}$ in the SPT. The stiffness of the secondary truss is 0.2 mm/g , the peak acceleration during scanning is $0.05g$ (4° s^{-2} 7 m from the azimuth axis) and the time to accelerate the telescope is $\sim 1 \text{ s}$, so scan-synchronous offsets are expected to be $\sim 100 \mu\text{K Hz}^{-1/2}$. Despite the fact that this is well below the detector noise, we discard data taken when the telescope is accelerating.

4. Telescope

4.1. Primary

The primary has 218 machined aluminum (Al Mg 4.5 Mn) panels mounted on a composite back up structure (BUS). The BUS is made of 24 identical, wedge-shaped segments that are essentially deep, stiff boxes with thick facesheets (see Figure 6). The segment walls have an aluminum honeycomb core covered with carbon-fiber-reinforced plastic (CFRP). Invar inserts are glued into the composite to provide attachment points for fasteners and panel adjusters. A large, stiff, Invar cone behind the BUS provides an interface to the steel telescope mount, and an Invar cylinder running from the center of the BUS to the steel mount adds axial stiffness.

Each aluminum panel is $\sim 0.5 \text{ m}^2 \times 60 \text{ mm}$ thick. The mass of each panel is reduced to $\sim 7 \text{ kg}$ by machining 20 to 40 pockets with 2 mm walls and leaving a 3 mm facesheet. The in-plane position of a panel is set by 3 horizontal adjusters. These have a post with an offset ball that engages a slot in the back of the panel. Panel position perpendicular to the BUS surface is controlled by 5 vertical adjusters, one near each corner of the panel and one near

the center. The vertical adjusters have a differential screw with a ~ 100 mm long \times 8 mm diameter rod that acts as a flexure. The adjusters were designed to give just a few μm rms deformation of the panels due to differential expansion of the panels and BUS. A 5-point vertical mount allows some bending to correct low-order surface profile errors, which are typically 10 μm . After setting all the vertical adjusters, the surface profile error of a single panel is 5–10 μm rms. The panels were initially installed on the BUS based on theodolite measurements of the positions of the panel corners. This gave a surface profile error of 240 μm rms. Adjustments based on photogrammetry measurements at EL= 45° reduced the surface error to 40 μm rms, and a final adjustment based on holography measurements at EL= 0° yielded a 20 μm rms surface (see Figure 5). Gravitational deflection of the primary contributes 11 μm rms surface error at the EL extremes (by calculation, after moving the receiver to the new focus position and assuming the primary was set at EL= 45°). Thermal deformation of the BUS is 1 μm rms (by calculation) for a temperature change of 35 K from the set point. The thermal effect is so small because the BUS and its Invar mounting adapters (which all have a low coefficient of thermal expansion) are attached to the steel mount with radial flexures (Hog 1975).

Gaps between panels are nominally 1 mm wide at -30° C (the temperature at which we assembled the primary), increasing to 2 mm at -80° C. The total gap area is $\sim 1\%$ of the primary, so the gaps would contribute ~ 2 K to the receiver noise and $\sim 1\%$ polarization errors. Both effects are a concern for CMB observations, so we covered the gaps with 5 mm wide \times 75 μm thick BeCu strips. These strips have spring fingers that engage the panel edges to pull the strip flat against the panel surface and center it in the gap (Padin et al. 2008). The cover strips contribute 11 μm rms, which increases the surface error of the primary from 20 to 23 μm rms. The panels were etched in NaOH to give a matte surface that scatters visible wavelengths. This reduces solar heating of the receiver cabin window to a few $\times 100$ W, preventing damage to the optics cryostat vacuum window if the telescope

is pointed at the Sun.

Ice on the primary would increase the receiver noise and scan-synchronous offsets, so the panels must be kept clean. Manual de-icing, e.g., brushing and scraping, is not practical for a 10 m telescope, so we have an electrical de-icing system with a 50 W m^{-2} flexible heating pad mounted behind each panel. Total power dissipation for the heater is 4 kW. This system runs continuously, raising the temperature of the panels 1–2 K above ambient, which is enough to discourage ice accumulation without significantly distorting the panels. Any ice that does form on the surface during a storm clears in about a day.

4.2. Mount

The SPT has an AZ-EL fork mount with both axes balanced to minimize deflections. The primary and receiver cabin are supported by a large, L-shaped frame with the EL axis and counterweight at the corner (see Figure 6). The EL bearings are spherical roller bearings mounted on the sides of the L frame, with stationary shafts that connect to the fork arms. The AZ bearing is a 3 m diameter roller bearing supported by a stiff (2 inch thick wall) cone tower. Space constraints in the offset design push the EL counterweight close to the EL axis, which makes for a large counterweight. The total mass of the SPT is $\sim 300,000 \text{ kg}$ and 20% of this is the counterweight. The structure breaks down into pieces that fit inside an LC130 aircraft for transportation to the South Pole, but welding on site is difficult so there are many flanges and bolts. These represent $\sim 20\%$ of the total mass.

The receiver cabin is a 5.5 m long \times 2.1 m wide \times 3.4 m high, insulated, shielded room on the end of the L frame. It moves with the telescope, but can be “docked” to the control room for work on the receiver. Large doors on the bottom of the cabin can be positioned above a sliding section of the control room roof. A retractable boot then seals the bottom

of the cabin to the outside of the roof. In the docked position, the cabin is essentially an extension of the control room, providing easy, warm access to the receiver and associated electronics. The docked configuration also provides a high ceiling for cryostat work that requires overhead lifting. The beam from the primary enters the cabin through a 12 mm thick expanded polypropylene foam window (Zotefoam PPA30). The window has a metal shutter covered with microwave absorber that can be used as an ambient load.

Ground shields are mounted along the L frame to reflect scattered radiation from the receiver window and primary to the sky. These shields are made of foam-core aluminum panels. Exposed edges are rolled with a radius of 3 cm, to reduce scattering, and gaps between the shields and primary are sealed with reflecting flashing. The shields have doors near the bottom of the primary to make snow removal easier. We did not install de-icing heaters on the shield panels, but we may add these in the future because manual de-icing is difficult.

The mount sits on a 5 m thick ice pad. This was built in 150 mm layers that were compacted by driving a bulldozer over each lift to give a density of 0.55–0.60 g cm⁻³. After construction, the ice was left to harden for a year. The ice now has a Young’s modulus of ~ 2 GPa and a compressive strength of ~ 0.5 MPa. The weight of the telescope is distributed by a large, wood raft. This is a regular hexagon, 6.4 m along each side, made of 150 × 300 mm timbers on 300 mm centers, with 19 mm plywood facesheets. It reduces the static pressure on the ice to ~ 28 kPa. Deflection of the ice and wood when the telescope accelerates is calculated to be ~ 1 arcsec. A 5.2 m high steel spaceframe tower supports the telescope on the raft. This tower helps to distribute the load, but its main function is to raise the telescope above snow grade to reduce drifting around the structure. The legs of the tower are insulated to reduce the cold load on the control room and deformation due to solar heating in summer.

4.3. Drive

Each axis has 4 brushless DC motors with gearboxes. These are mounted in pairs, with a torque bias between the motors in each pair to eliminate backlash. The 2 pairs of AZ motors are mounted on opposite sides of the fork and they engage an external ring gear on the AZ bearing. Each arm of the fork has a pair of EL motors that drive a sector gear mounted on the L frame. All the motors have disc brakes that can stop the motor shaft at full torque. The L frame also has hard stops with shock absorbers. The drive can operate at reduced speed with just 2 motors per axis in the event of a failure. Both axes have 26-bit optical encoders (BEI model LS898⁵). The AZ encoder is mounted at the base of the cone tower on a reference frame attached to the foundation mounting pads. It has a ~ 2 m long shaft/flexure that passes through the helical-spring AZ cable wrap to the bottom of the fork. There are 2 EL encoders, one in each fork arm, and they also have a ~ 2 m long shaft/flexure that runs through the EL bearing to the L frame. Performance details for the drive are given in Table 1. The SPT can scan between 2 positions 1° apart, settling within 3 arcsec of the requested position in 3 s. During a scan, it can follow the commanded path within 20 arcsec at accelerations up to 2° s^{-2} (with better performance at lower accelerations). Figure 7 shows recorded telescope position and tracking errors during a typical CMB field scan. The actual path can always be reconstructed within 1 arcsec using the encoder readings.

A metrology system measures changes in the overall tilt of the mount and deformations in the fork structure. There are 3 metrology subsystems:

- (1) A biaxial tiltmeter (Applied Geomechanics model 711-2A⁶) mounted on the pedestal

⁵BEI Sensors & Systems Company, Maumelle AK 72113

⁶Applied Geomechanics Inc., Santa Cruz CA 95062

wall measures changes in the tilt of the AZ axis, which are mainly due to settling of the foundation. We have a second tiltmeter in the fork, just above the center of the AZ bearing, to measure repeatable tilts in the bearing. These are ~ 5 arcsec p-p and they are recorded in a look-up table which can be applied in the on-line pointing model.

(2) EL encoders in each fork arm measure twisting of the L frame and forks. The average of the two encoder readings provides the elevation position feedback to the drive system and the difference is used to calculate the AZ error due to twisting.

(3) A pair of linear displacement sensors (BEI model LGDT-5⁷) mounted on each fork arm measure changes in the height and rotation of the arms relative to a stiff, CFRP reference frame inside the fork (see Figure 8). Rotations of the fork arms cause AZ and EL offsets and changes in height tilt the EL axis.

Metrology corrections can be applied in the telescope control system, based on a 10 s running average of the sensor readings. This ensures stability and low noise, but it means we cannot correct deflections due to fast motion of the telescope.

The SPT has an optical star pointing system for measuring axis tilts, encoder offsets and gravitational flexure. Two 75 mm near-IR refractors are mounted on the edge of the BUS (at 12 and 3 o'clock) and a 3rd is mounted on the end of the L frame by the receiver cabin. The pointing telescopes have CCD video cameras connected to a frame grabber in the telescope control computer. We can automatically measure pointing errors for about 30 bright stars in half an hour. The rms pointing error in one of these runs is typically 3 arcsec (see Figure 9), but the best fit model varies by a few tens of arcsec on timescales of a day. This appears to be due mainly to complicated thermal deformation of the fork arms, so we have improved the insulation and have installed temperature sensors to measure thermal

⁷BEI Sensors & Systems Company, Maumelle AK 72113

gradients in the fork. We have implemented a radio pointing model which combines the information from the temperature sensors, the linear displacement sensors, and observations of galactic H II regions. This model confirms the drifts seen in the star camera observations, and with it we are able to correct for these drifts and reconstruct pointing with ~ 10 -arcsec rms on hour timescales (which is the typical separation between H II region measurements). We have no evidence of pointing drifts on shorter timescales than this.

The telescope control system is based on software written for the Sunyaev-Zel'dovich Array (SZA). Requested (AZ,EL) positions (including precession, refraction, mount errors etc.) are computed every 10 ms and sent to the drive. Encoder readings and status information (motor currents, faults etc.) are recorded every 10 ms. Scanning is implemented by adding offsets from a table to the requested (AZ,EL). Most observations are managed by scripts containing high-level control commands (e.g., wait until a particular time and then start a series of scans on the target source, or drive to stow if the receiver temperature is above some threshold).

The drive motors, brakes, gearboxes, encoders and limit switches are all warm to improve reliability, and they are easily accessible from the control room, so they can be repaired in winter when it is difficult to work outside. The cone tower and the bottom of the fork are inside the control room, which has a rotating roof attached to the fork. The fork arms are enclosed by insulated cabins (riding on top of the rotating roof) with openings to the control room below. The only cold drive parts are the EL sector gears and the EL bearings.

5. Receiver

5.1. Focal plane

The detectors in the SPT receiver (Shirokoff et al. in prep.) are arrays of horn-coupled, spider-web bolometers with TES thermometers (Gildemeister et al. 1999; Gildemeister et al. 2000). A voltage-biased TES exhibits strong electrothermal feedback, resulting in good linearity and a responsivity that is independent of bath temperature and optical loading (Lee et al. 1996; Lee et al. 1998). The TES devices also have low impedance (typically 1Ω), so they should be fairly insensitive to vibrationally induced currents. In addition, the resonant circuits in series with each bolometer (see Section 5.2) pass only a narrow band of signals at several hundred kHz where there are no mechanical excitations.

The SPT detectors have an Al-Ti TES, with a transition temperature of ~ 0.5 K, mounted near the center of a spiderweb absorber. This absorber is a $1\ \mu\text{m}$ thick, suspended silicon nitride mesh, 3 mm in diameter suspended by six 0.5 mm legs. It is coated with gold to give a sheet resistance of a few $100\Omega/\square$. High electrothermal loop gain leads to a short electrical time constant that can cause instability (Irwin et al. 1998), so our detectors also have a gold pad coupled to the TES to increase its heat capacity and slow its electrical time constant. We use triangular arrays of 161 close-packed bolometers (see Figure 10) fabricated on 100 mm diameter wafers. The wafers are metallized on the back to provide a backshort at $\sim \lambda/4$. The bands are defined by the low-frequency cut off in a short length of circular waveguide between each smooth-wall conical horn and its detector, and by low-pass, metal-mesh filters (Ade et al. 2006) mounted in front of each feedhorn array. The focal plane has 6 triangular bolometer arrays, for a total of 966 detectors; however, due to readout limitations at most 840 detectors can be active.

For the 2009 season, one $\lambda = 3$ mm array, four 2 mm arrays and two 1.3 mm arrays

have been installed. Typically, ~ 700 detectors pass our performance cuts with high sensitivity and noise close to the background limit. The typical optical coupling from the sky to the TES is $\sim 25\%$. The mean noise equivalent CMB temperatures (NET) and yields for each of the three bands in the 2009 SZ receiver configuration are summarized in Table 2.

The NETs quoted in Table 2 are evaluated at ~ 3 Hz (or $\ell \simeq 2000$ to 4000 for typical scan speeds). At lower frequencies, single-detector noise levels rise due to atmosphere and, to a lesser degree, detector and readout $1/f$ noise. Figure 11 shows NET as a function of (temporal) frequency for typical detectors at each observing wavelength under typical observing conditions. NET is shown for data taken while scanning and while stationary. The slight increase in low-frequency noise while scanning is due to the faster imaging of large-angle atmospheric fluctuations.

For a typical detector, the optical time constant is ~ 15 ms. For typical SPT scan speeds of 0.25 to 0.5 degrees/s, this implies a 3 dB spatial frequency of $\ell \simeq 7500$ to 15000. For comparison, the 3 dB point of a 1 arcmin beam is $\ell \simeq 6700$; i.e., the detector time constants are not limiting our high- ℓ response at typical scan speeds. Furthermore, in the regime in which photon shot noise is the dominant contribution to the detector noise budget, the noise is rolled off with the optical time constant just as the signal is, and the signal-to-noise ratio does not decrease (Lee et al. 1998). Most of the SPT detectors operate in or near this regime, so much faster scanning is feasible from a detector noise standpoint.

5.2. Cryogenics

The SPT receiver (Benson et al., in prep) is cooled by a pulse tube refrigerator (model PT415⁸) with capacity of 1.5 W at 4.2 K and 40 W at 45 K, and a 3-stage $^4\text{He}^3\text{He}^3\text{He}$

⁸Cryomech Inc., Syracuse NY 13211

sorption refrigerator (model CRC10⁹) with a capacity of 80 μW at 380 mK and 4 μW at 250 mK. The sub-K refrigerator is cycled automatically in ~ 3 hrs and the hold time is ~ 36 hrs.

5.3. Readout

The SPT receiver readout (Dobbs et al. in prep) is a frequency multiplexed SQUID readout with 8 detectors per SQUID (Spieler 2002; Lanting et al. 2005). Each TES is biased with a constant voltage amplitude sine wave, in the 0.3–1 MHz range, and has a series LC filter, mounted near the focal plane at 250 mK, to select the appropriate bias frequency from a comb of 8 (see Figure 12). In this scheme, only 2 superconducting NbTi wires are needed to connect 8 detectors in the focal plane to their SQUID, which is mounted at 4 K. The LC filters all have 16 μH chip inductors, so the filter Q increases with frequency and the bandwidth (~ 5 kHz in the SPT) is constant. The filter frequency is set by the capacitor, which is a standard ceramic chip device. The SQUIDs are 100-element series arrays (Huber et al. 2001) with a small input coil to reduce pickup of spurious signals. These devices have 120 MHz bandwidth, 500 V/A transimpedance and the noise (referred to the input coil) is 2.5 pA Hz^{-1/2} (cf. ~ 15 pA Hz^{-1/2} bolometer noise). SQUIDs are extremely sensitive to magnetic fields, so the SQUID boards (each with 8 SQUID arrays) are enclosed in a Cryoperm shield to attenuate any external fields. Inside the cryoperm shield, each SQUID is mounted on a Nb film (type 2 superconductor) to pin any residual magnetic flux. To maintain constant voltage bias across the TES, the input impedance of the SQUID must be small compared with the TES resistance. This requires that the SQUID be operated with shunt feedback from the output of the room-temperature amplifier that follows. Negative

⁹Chase Research Cryogenics Ltd., Sheffield S10 5DL UK

feedback also linearizes the SQUID response, reducing intermodulation between the bias signals. The feedback amplifier has a high gain \times bandwidth product, so connections between the SQUID and the room temperature electronics must be short. This is a severe constraint on the mechanical and thermal design of the receiver.

Bias signals for the detectors are generated by direct digital synthesizers with low sideband noise. The SQUID amplifier outputs are demodulated by square-wave mixers, which have low distortion because they contain no non-linear components. The demodulated signals are filtered by 8-pole, low-pass, anti-aliasing filters and then digitized with 14 bits resolution. All the bias synthesizers and demodulator electronics are on 9U VME cards with 16 channels per card. Each card has a field programmable gate array that packages the data with a time tag and provides control and monitoring of the readout configuration. The electronics for a 966-pixel receiver occupy 3 VME crates (see Figure 13).

6. Observations

Most SPT observations involve scanning the telescope to fully sample the sky with all the detectors (and hence all of the frequency bands). We generally scan back and forth in AZ at constant speed, turning around as quickly as possible, with a step in EL at the end of each AZ scan. The speed in the linear part of the AZ scan involves a trade off between noise and observing efficiency. Higher scan speeds move the sky signals to higher frequency in the detector timestreams, so low-frequency noise from the atmosphere and receiver become less important, but the observing efficiency is reduced because a larger fraction of the time is spent turning around. Typical scan speeds for large CMB fields have ranged

from 0.25 to 0.5 degrees/s.¹⁰ The EL steps at the end of each scan are profiled to minimize the excitation of elevation oscillations, which would lead to scan synchronous modulations of the atmosphere.

A typical observation starts with a small (~ 2 degree) scan in EL (to inject a signal from the atmosphere), followed by observations of a chopped thermal source and H II regions. In Figure 14 we show the SPT images of one of the galactic HII regions used, RCW38. This set of calibration observations allows us to measure the detector gains and monitor the opacity of the atmosphere. The chopped thermal source is a ~ 1000 K black-body, with a 4–100 Hz chopper wheel, connected to a 9.5 mm diameter light pipe that runs into the optics cryostat and through a hole in the center of the secondary. We check the pointing by mapping two bright H II regions near the target field, which takes ~ 20 min total, and then we scan on the target field for a few hours. The cycle is repeated until the mK refrigerator in the receiver warms up. Detector outputs and telescope positions are recorded at 100 Hz, but most of the monitoring (e.g., cryostat temperatures, weather, receiver readout configuration and optical bench position) is at 1 Hz. The data rate is typically 30 GBytes/day and all the data are returned to the US via NASA’s Tracking and Data Relay Satellite System.

About half of our 1st year (2007) observations were performance tests (e.g., measurements of beams, focus, pointing, ground pickup and detector noise and time constants). The rest of the year was spent on a deep observation of a ~ 7 deg² field and a ~ 50 deg² field to search for galaxy clusters via the SZ effect and to measure the high- l angular power spectrum of the CMB. The second year observations concentrated primarily

¹⁰Scan speeds are quoted here in terms of geodesic distance; speeds in units of degrees of azimuth per second will be higher by a factor of one over the cosine of the observing elevation.

on SZ and fine-scale CMB surveys in two ~ 100 deg² fields. Targeted SZ observations toward known galaxy clusters were also pursued. Since the beginning of the third observing season, we have spent the vast majority of time on the survey and are currently mapping the sky to survey depth at a speed of over 700 deg² yr⁻¹. We reported the first clusters detected via their SZ signature in Staniszewski et al. (2009) and have since published many significant results, including the first SZ-selected cluster catalog and cosmological constraints from that catalog, the first detection of the power spectrum of secondary CMB anisotropy, a point-source catalog that includes an exciting new population of high-redshift sources, and observations of the SZ effect in known galaxy clusters out to unprecedented clustercentric radii (Vanderlinde et al. 2010; Lueker et al. 2010; Vieira et al. 2010; Plagge et al. 2010).

7. Conclusions

The South Pole Telescope (SPT), a 10 m diameter, wide-field, offset Gregorian telescope equipped with a 966-pixel millimeter-wave bolometer camera, has been successfully deployed at the Amundsen-Scott South Pole station. The SPT has been operating at the South Pole since February 2007. It has a simple, low-loss optical system, with good control of spillover and scattered radiation. Low noise, small offsets and high throughput, combined with the exceptional transparency and stability of the South Pole atmosphere, makes the instrument ideal for survey work and observations of low surface brightness emission, such as the CMB. The telescope has a 20 μ m rms surface, and pointing errors of a few arcsec, so it can be used at submillimeter wavelengths.

The first key project of the SPT is a large scale survey of the sky (1000's of sq. degrees) at 3, 2 and 1.3 mm to search for the galaxy clusters via the SZ effect and to measure the fine-scale anisotropy of the CMB. The SZ receiver is now operating with background limited

performance in all three observing bands.

This paper offers a snapshot of the current status of the SPT. Throughout the life of the telescope it is expected that several receivers will be deployed for conducting major large-scale survey projects at millimeter through submillimeter wavelengths. We are currently building a polarimeter for measuring the B-mode polarization anisotropy of the CMB.

We thank R. Hills for many useful discussions on the optical design. We gratefully acknowledge the contributions to the construction of the telescope from T. Hughes, P. Huntley, B. Johnson and E. Nichols and his team of iron workers. We also thank the National Science Foundation (NSF) Office of Polar Programs, the United States Antarctic Program and the Raytheon Polar Services Company for their support of the project. We are grateful for professional support from the staff of the South Pole station. The SPT is supported by the National Science Foundation through grants ANT-0638937 and ANT-0130612. Partial support is also provided by the NSF Physics Frontier Center grant PHY-0114422 to the Kavli Institute of Cosmological Physics at the University of Chicago, the Kavli Foundation and the Gordon and Betty Moore Foundation. The McGill group acknowledges funding from the National Sciences and Engineering Research Council of Canada, the Quebec Fonds de recherche sur la nature et les technologies, and the Canadian Institute for Advanced Research. The following individuals acknowledge additional support: J. Carlstrom from the James S. McDonnell Foundation, K. Schaffer from a KICP Fellowship, J. McMahon from a Fermi Fellowship, Z. Staniszewski from a GAAN Fellowship, and A.T. Lee from the Miller Institute for Basic Research in Science, University of California Berkeley.

REFERENCES

- Ade, P. A. R., Pisano, G., Tucker, C., & Weaver, S. 2006, in Society of Photo-Optical Instrumentation Engineers (SPIE) Conference Series, Vol. 6275, Society of Photo-Optical Instrumentation Engineers (SPIE) Conference Series
- Bussmann, R. S., Holzapfel, W. L., & Kuo, C. L. 2005, *ApJ*, 622, 1343
- Carlstrom, J. E., Holder, G. P., & Reese, E. D. 2002, *ARA&A*, 40, 643
- Chamberlin, R. A. 2001, *J. Geophys. Res. Atmospheres*, 106 (D17), 20101
- Crittenden, R., Davis, R. L., & Steinhardt, P. J. 1993, *ApJ*, 417, L13
- Dragone, C. 1982, *IEEE Transactions on Antennas and Propagation*, 30, 331
- Dunkley, J., Komatsu, E., Nolta, M. R., Spergel, D. N., Larson, D., Hinshaw, G., Page, L., Bennett, C. L., Gold, B., Jarosik, N., Weiland, J. L., Halpern, M., Hill, R. S., Kogut, A., Limon, M., Meyer, S. S., Tucker, G. S., Wollack, E., & Wright, E. L. 2009, *ApJS*, 180, 306
- Gildemeister, J. M., Lee, A. T., & Richards, P. L. 1999, *Applied Physics Letters*, 74, 868
- . 2000, *Applied Physics Letters*, 77, 4040
- Griffin, M. J., Bock, J. J., & Gear, W. K. 2002, *Appl. Opt.*, 41, 6543
- Hanany, S. & Marrone, D. P. 2002, *Applied Optics*, 41, 4666
- Hog, E. 1975, *A&A*, 41, 107
- Holder, G., Haiman, Z., & Mohr, J. J. 2001, *ApJ*, 560, L111

- Holland, W., Duncan, W., & Griffin, M. 2002, in *Astronomical Society of the Pacific Conference Series*, Vol. 278, *Single-Dish Radio Astronomy: Techniques and Applications*, ed. S. Stanimirovic, D. Altschuler, P. Goldsmith, & C. Salter, 463–491
- Hu, W. & Dodelson, S. 2002, *ARA&A*, 40, 171
- Huber, M., Neil, P., Benson, R., Burns, D., Corey, A., Flynn, C., Kitaygorodskaya, Y., Massihzadeh, O., Martinis, J., & Hilton, G. 2001, *IEEE Transactions on Applied Superconductivity*, 11, 4048
- Irwin, K. D., Hilton, G. C., Wollman, D. A., & Martinis, J. M. 1998, *Journal of Applied Physics*, 83, 3978
- Knox, L. & Song, Y. 2002, *Physical Review Letters*, 89, 011303
- Komatsu, E. & Seljak, U. 2002, *MNRAS*, 336, 1256
- Kovac, J. M., Leitch, E. M., Pryke, C., Carlstrom, J. E., Halverson, N. W., & Holzappel, W. L. 2002, *Nature*, 420, 772
- Lanting, T. M., Cho, H.-M., Clarke, J., Holzappel, W. L., Lee, A. T., Lueker, M., Richards, P. L., Dobbs, M. A., Spieler, H., & Smith, A. 2005, *Applied Physics Letters*, 86, 2511
- Lee, A. T., Richards, P. L., Nam, S. W., Cabrera, B., & Irwin, K. D. 1996, *Applied Physics Letters*, 69, 1801
- Lee, S., Gildemeister, J. M., Holmes, W., Lee, A. T., & Richards, P. L. 1998, *Appl. Opt.*, 37, 3391
- Lueker, M., Reichardt, C. L., Schaffer, K. K., Zahn, O., Ade, P. A. R., Aird, K. A., Benson, B. A., Bleem, L. E., Carlstrom, J. E., Chang, C. L., Cho, H. M., Crawford, T. M., Crites, A. T., de Haan, T., Dobbs, M. A., George, E. M., Hall, N. R., Halverson,

- N. W., Holder, G. P., Holzzapfel, W. L., Hrubes, J. D., Joy, M., Keisler, R., Knox, L., Lee, A. T., Leitch, E. M., McMahon, J. J., Mehl, J., Meyer, S. S., Mohr, J. J., Montroy, T. E., Padin, S., Plagge, T., Pryke, C., Ruhl, J. E., Shaw, L., Shirokoff, E., Spieler, H. G., Staniszewski, Z., Stark, A. A., Vanderlinde, K., Vieira, J. D., & Williamson, R. 2010, *ApJ*, 719, 1045
- Nolta, M. R., Dunkley, J., Hill, R. S., Hinshaw, G., Komatsu, E., Larson, D., Page, L., Spergel, D. N., Bennett, C. L., Gold, B., Jarosik, N., Odegard, N., Weiland, J. L., Wollack, E., Halpern, M., Kogut, A., Limon, M., Meyer, S. S., Tucker, G. S., & Wright, E. L. 2009, *ApJS*, 180, 296
- Okamoto, T. & Hu, W. 2003, *Phys. Rev. D*, 67, 083002
- Padin, S., Carlstrom, J. E., Chauvin, E., & Busetti, S. 2008, *Electronics Letters*, 44, 950
- Padin, S., Staniszewski, Z., Keisler, R., Joy, M., Stark, A. A., Ade, P. A. R., Aird, K. A., Benson, B. A., Bleem, L. E., Carlstrom, J. E., Chang, C. L., Crawford, T. M., Crites, A. T., Dobbs, M. A., Halverson, N. W., Heimsath, S., Hills, R. E., Holzzapfel, W. L., Lawrie, C., Lee, A. T., Leitch, E. M., Leong, J., Lu, W., Lueker, M., McMahon, J. J., Meyer, S. S., Mohr, J. J., Montroy, T. E., Plagge, T., Pryke, C., Ruhl, J. E., Schaffer, K. K., Shirokoff, E., Spieler, H. G., & Vieira, J. D. 2008, *Appl. Opt.*, 47, 4418
- Page, L., Hinshaw, G., Komatsu, E., Nolta, M. R., Spergel, D. N., Bennett, C. L., Barnes, C., Bean, R., Doré, O., Dunkley, J., Halpern, M., Hill, R. S., Jarosik, N., Kogut, A., Limon, M., Meyer, S. S., Odegard, N., Peiris, H. V., Tucker, G. S., Verde, L., Weiland, J. L., Wollack, E., & Wright, E. L. 2007, *ApJS*, 170, 335
- Plagge, T., Benson, B. A., Ade, P. A. R., Aird, K. A., Bleem, L. E., Carlstrom, J. E., Chang, C. L., Cho, H., Crawford, T. M., Crites, A. T., de Haan, T., Dobbs, M. A.,

- George, E. M., Hall, N. R., Halverson, N. W., Holder, G. P., Holzapfel, W. L., Hrubes, J. D., Joy, M., Keisler, R., Knox, L., Lee, A. T., Leitch, E. M., Lueker, M., Marrone, D., McMahon, J. J., Mehl, J., Meyer, S. S., Mohr, J. J., Montroy, T. E., Padin, S., Pryke, C., Reichardt, C. L., Ruhl, J. E., Schaffer, K. K., Shaw, L., Shirokoff, E., Spieler, H. G., Stalder, B., Staniszewski, Z., Stark, A. A., Vanderlinde, K., Vieira, J. D., Williamson, R., & Zahn, O. 2010, *ApJ*, 716, 1118
- Polnarev, A. G. 1985, *Soviet Ast.*, 29, 607
- Richards, P. L. 1994, *Journal of Applied Physics*, 76, 1
- Ruhl, J., Ade, P. A. R., Carlstrom, J. E., Cho, H.-M., Crawford, T., Dobbs, M., Greer, C. H., Halverson, N. W., Holzapfel, W. L., Lanting, T. M., Lee, A. T., Lerlinitch, E. M., Leong, J., Lu, W., Lueker, M., Mehl, J., Meyer, S. S., Mohr, J. J., Padin, S., Plagge, T., Pryke, C., Runyan, M. C., Schwan, D., Sharp, M. K., Spieler, H., Staniszewski, Z., & Stark, A. A. 2004, in *Proc. SPIE, Vol. 5498, Millimeter and Submillimeter Detectors for Astronomy II*, ed. J. Zmuidzinas, W. S. Holland, & S. Withington (Bellingham: SPIE Optical Engineering Press), 11–29
- Sayers, J., Golwala, S. R., Ade, P. A. R., Aguirre, J. E., Bock, J. J., Edgington, S. F., Glenn, J., Goldin, A., Haig, D., Lange, A. E., Laurent, G. T., Mauskopf, P. D., Nguyen, H. T., Rossinot, P., & Schlaerth, J. 2010, *ApJ*, 708, 1674
- Schwerdtfeger, W. 1984, *Weather and Climate of the Antarctic* (Amsterdam: Elsevier)
- Seljak, U. 1997, *ApJ*, 482, 6
- Seljak, U. & Zaldarriaga, M. 1997, *Physical Review Letters*, 78, 2054
- Spieler, H. 2002, in *Monterey Far-IR, Sub-mm and mm Detector Technology Workshop proceedings*, ed. J. Wolf, J. Farhoomand, & C. McCreight, 243–249

- Staniszewski, Z., Ade, P. A. R., Aird, K. A., Benson, B. A., Bleem, L. E., Carlstrom, J. E., Chang, C. L., Cho, H.-M., Crawford, T. M., Crites, A. T., de Haan, T., Dobbs, M. A., Halverson, N. W., Holder, G. P., Holzzapfel, W. L., Hrubes, J. D., Joy, M., Keisler, R., Lanting, T. M., Lee, A. T., Leitch, E. M., Loehr, A., Lueker, M., McMahon, J. J., Mehl, J., Meyer, S. S., Mohr, J. J., Montroy, T. E., Ngeow, C.-C., Padin, S., Plagge, T., Pryke, C., Reichardt, C. L., Ruhl, J. E., Schaffer, K. K., Shaw, L., Shirokoff, E., Spieler, H. G., Stalder, B., Stark, A. A., Vanderlinde, K., Vieira, J. D., Zahn, O., & Zenteno, A. 2009, *ApJ*, 701, 32
- Sunyaev, R. A. & Zel'dovich, Y. B. 1972, *Comments on Astrophysics and Space Physics*, 4, 173
- Tegmark, M. 2005, *Physica Scripta Volume T*, 121, 153
- Tucker, C. E. & Ade, P. A. R. 2006, in *Society of Photo-Optical Instrumentation Engineers (SPIE) Conference Series*, Vol. 6275, *Society of Photo-Optical Instrumentation Engineers (SPIE) Conference Series*
- Vanderlinde, K., Crawford, T. M., de Haan, T., Dudley, J. P., Shaw, L., Ade, P. A. R., Aird, K. A., Benson, B. A., Bleem, L. E., Brodwin, M., Carlstrom, J. E., Chang, C. L., Crites, A. T., Desai, S., Dobbs, M. A., Foley, R. J., George, E. M., Gladders, M., Hall, N. R., Halverson, N. W., High, F. W., Holder, G. P., Holzzapfel, W. L., Hrubes, J. D., Joy, M., Keisler, R., Knox, L., Lee, A. T., Leitch, E. M., Loehr, A., Lueker, M., Marrone, D. P., McMahon, J. J., Mehl, J., Meyer, S. S., Mohr, J. J., Montroy, T. E., Ngeow, C.-C., Padin, S., Plagge, T., Pryke, C., Reichardt, C. L., Rest, A., Ruel, J., Ruhl, J. E., Schaffer, K. K., Shirokoff, E., Song, J., Spieler, H. G., Stalder, B., Staniszewski, Z., Stark, A. A., Stubbs, C. W., van Engelen, A., Vieira, J. D., Williamson, R., Yang, Y., Zahn, O., & Zenteno, A. 2010, *ApJ*, 722, 1180

Vieira, J. D., Crawford, T. M., Switzer, E. R., Ade, P. A. R., Aird, K. A., Ashby, M. L. N., Benson, B. A., Bleem, L. E., Brodwin, M., Carlstrom, J. E., Chang, C. L., Cho, H., Crites, A. T., de Haan, T., Dobbs, M. A., Everett, W., George, E. M., Gladders, M., Hall, N. R., Halverson, N. W., High, F. W., Holder, G. P., Holzappel, W. L., Hrubes, J. D., Joy, M., Keisler, R., Knox, L., Lee, A. T., Leitch, E. M., Lueker, M., Marrone, D. P., McIntyre, V., McMahon, J. J., Mehl, J., Meyer, S. S., Mohr, J. J., Montroy, T. E., Padin, S., Plagge, T., Pryke, C., Reichardt, C. L., Ruhl, J. E., Schaffer, K. K., Shaw, L., Shirokoff, E., Spieler, H. G., Stalder, B., Staniszewski, Z., Stark, A. A., Vanderlinde, K., Walsh, W., Williamson, R., Yang, Y., Zahn, O., & Zenteno, A. 2010, *ApJ*, 719, 763

Wilson, R. N. 1996, *Reflecting Telescope Optics I. Basic Design Theory and its Historical Development*. (Springer)

Table 1: Drive performance.

Parameter	AZ	EL	Units
Range	± 270	0–140	deg
Maximum speed	4	2	deg s ⁻¹
Maximum acceleration	4	4	deg s ⁻²
Drive gear ratio	9.319	13.410	
Motor gearbox ratio	579	894	
Motor speed	3600	4000	rpm
Motor torque	33	33	ft lb
Motor inertia	0.016	0.016	ft lb s ²
Structure inertia	1.69×10^6	2.15×10^6	ft lb s ²
Structure inertia at motor shaft	0.058	0.015	ft lb s ²
Resonant Frequency	3.7	2.5	Hz

Table 2: 2009 SZ Receiver Performance

Band (mm)	Typical # Active Bolometers	Typical NET (μ K _{CMB} \sqrt{s})
3	120	600
2	465	450
1.3	100	1200



Fig. 1.— The 10 meter South Pole Telescope (SPT).

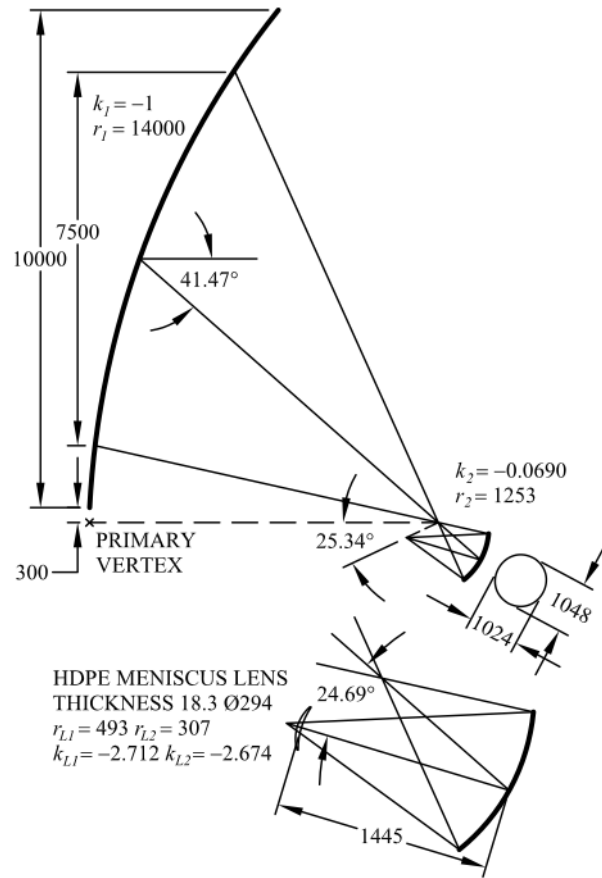


Fig. 2.— SPT optics details for (top) the basic Gregorian telescope with no lens and (bottom) a meniscus lens that makes the final focus telecentric and gives more uniform illumination of the secondary. For each surface, r is the radius of curvature and k is the conic constant. Dimensions are in mm at the operating temperature (ambient for the primary, 10 K for the secondary and 4 K for the lens).

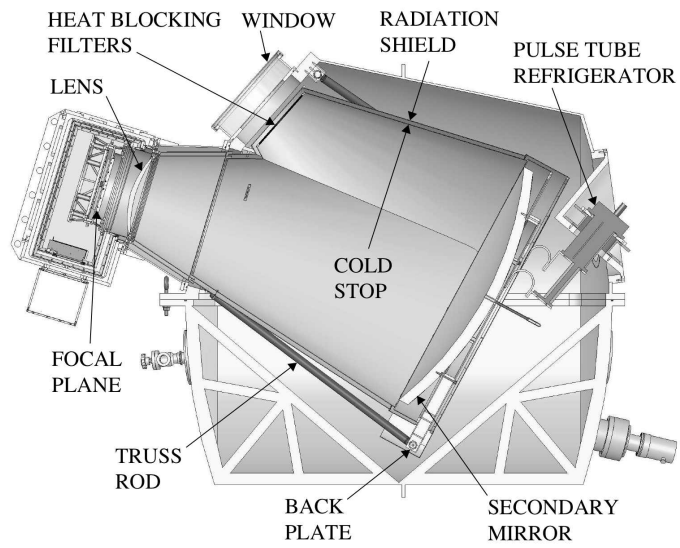


Fig. 3.— Section through the receiver and optics cryostats.



Fig. 4.— Optical bench assembly. This view is looking up into the receiver cabin from the control room. The sky end of the cabin is at the top. The optics cryostat is the large, white, cylindrical vessel in the center of the picture and the optical bench is the white frame around it. The receiver (with many wires running down to the readout electronics) is just below center. Three of the 6 optical bench actuators are visible at the top, left and right of the picture. The other 3 actuators connect the corners of the bench to the cabin roof.

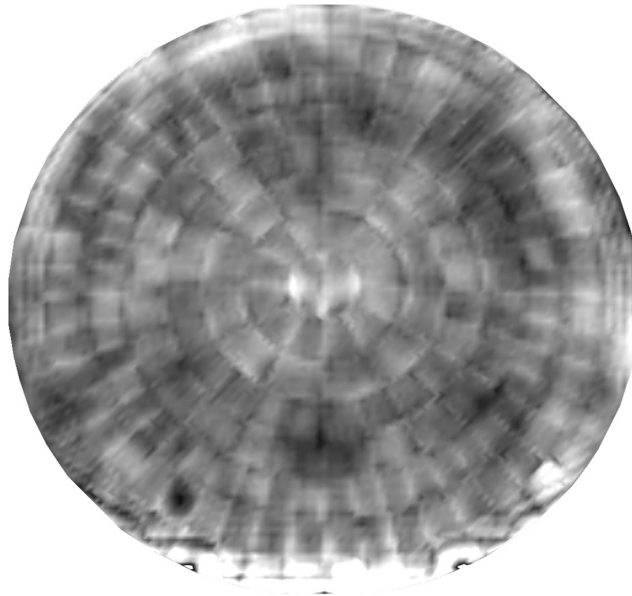


Fig. 5.— Primary surface profile errors. The greyscale range is $+75 \mu\text{m}$ (white) to $-75 \mu\text{m}$ (black). The features at the bottom are artifacts caused by reflections from the L frame where the beam enters the receiver cabin near prime focus. Light (i.e., high) stripes along the panel edges are due to the gap covers. The surface error (with uniform weighting over the entire primary) is $20 \mu\text{m}$ rms.

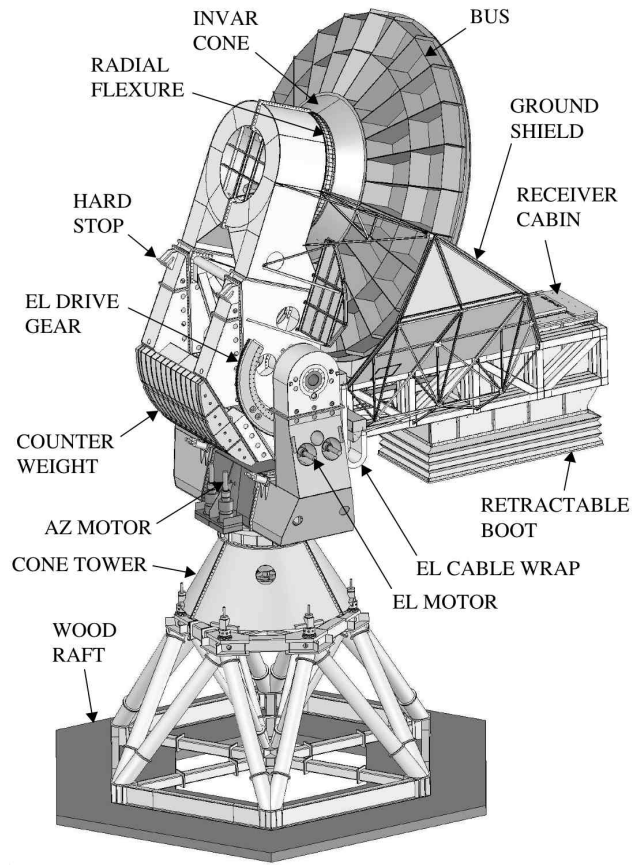


Fig. 6.— Mount details. The receiver cabin, fork cabins, control room rotating roof and the covers on the back of the BUS have been removed to show the telescope structure.

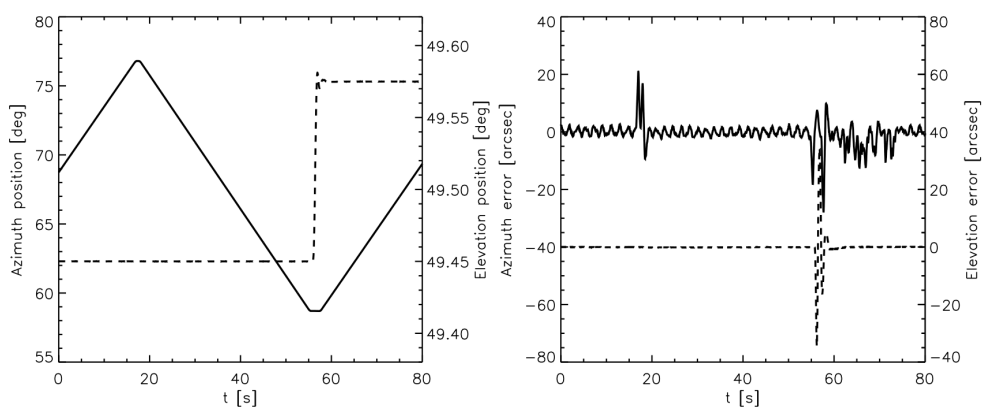


Fig. 7.— Recorded telescope position and tracking errors (recorded position minus commanded position) during a typical CMB field scan. In both plots, the solid line is azimuth, and the dashed line is elevation. (Note the different scales for azimuth and elevation position and the offset between the azimuth and elevation error axes). Tracking errors briefly exceed 20 arcsec during azimuth turnarounds and elevation steps, but they quickly settle to well below the 20-arcsec specification and remain so throughout the constant-velocity portion of the scan.

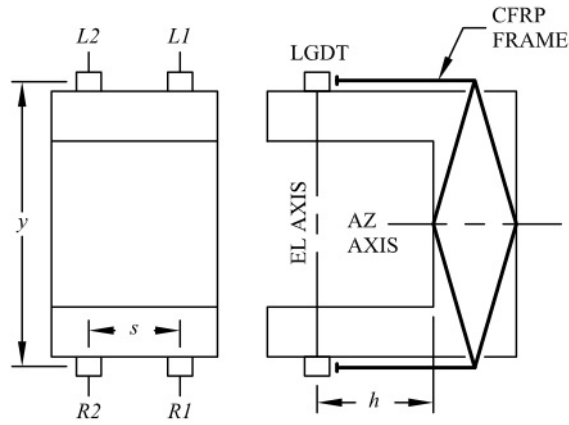


Fig. 8.— Fork metrology system. LGDT is a linear gap displacement transducer. $L1$, $L2$, $R1$ and $R2$ are distances (measured parallel to the AZ axis) from points on the fork to the CFRP frame. If $L1$ and $R1$ are on the receiver cabin side of the fork, the corrections for AZ and EL offsets and EL axis tilt are $\Delta AZ = (L1 - L2 - R1 + R2) h / y s$, $\Delta EL = (L2 - L1 + R2 - R1) / 2s$ and $\Delta ET = (L1 + L2 - R1 - R2) / 2y$ radians.

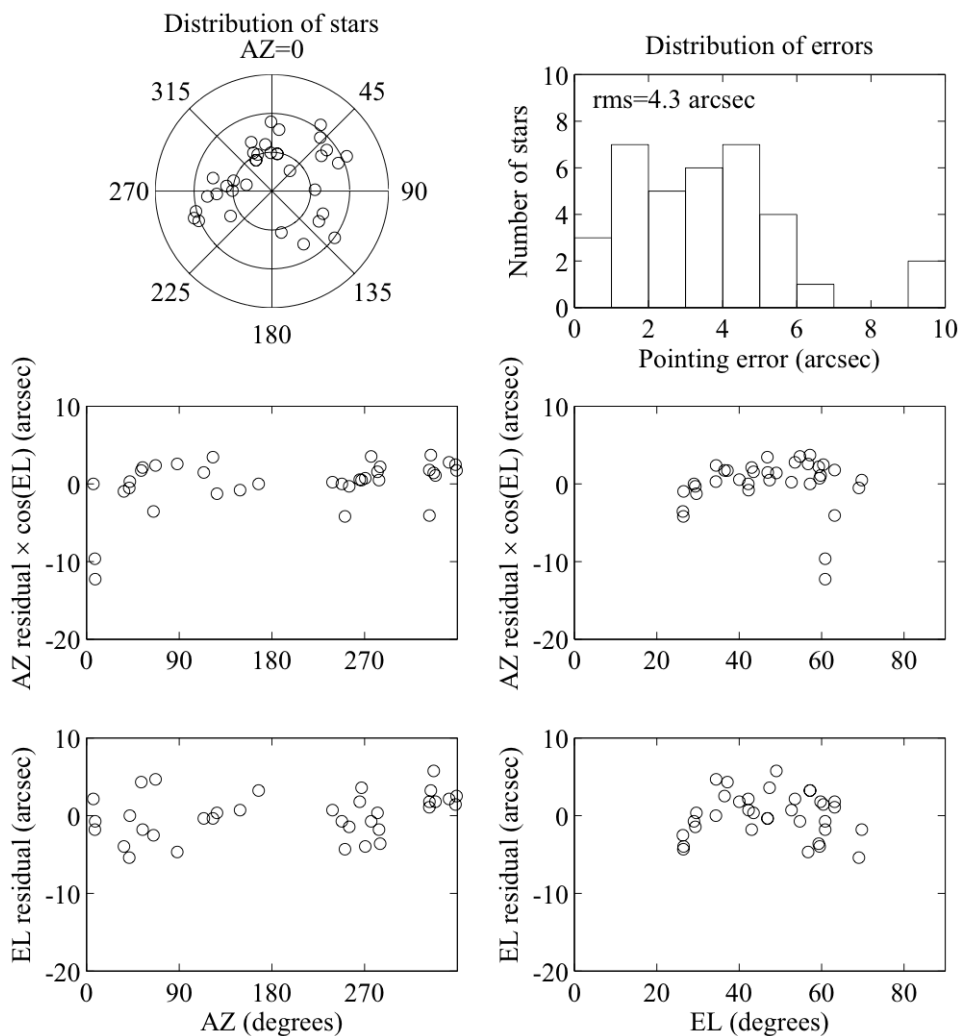


Fig. 9.— Pointing errors measured with the optical telescope on the end of the L frame. This observation of 35 stars was made on 17-Jun-2007 at 23:08 UT. The plots show AZ and EL residuals after fitting for AZ and EL axis tilts, AZ and EL encoder offsets, $\sin(\text{EL})$ and $\cos(\text{EL})$ flexure and optical telescope cross-EL collimation. The rms of the residuals is 4.3 arcsec, but this includes ~ 3 arcsec rms seeing, so the mount errors are ~ 3 arcsec rms. The 2 outliers near $\text{AZ} = 0$ are in the Alpha Centauri system. They consistently have high AZ residuals, possibly because of an error in the proper motion correction.

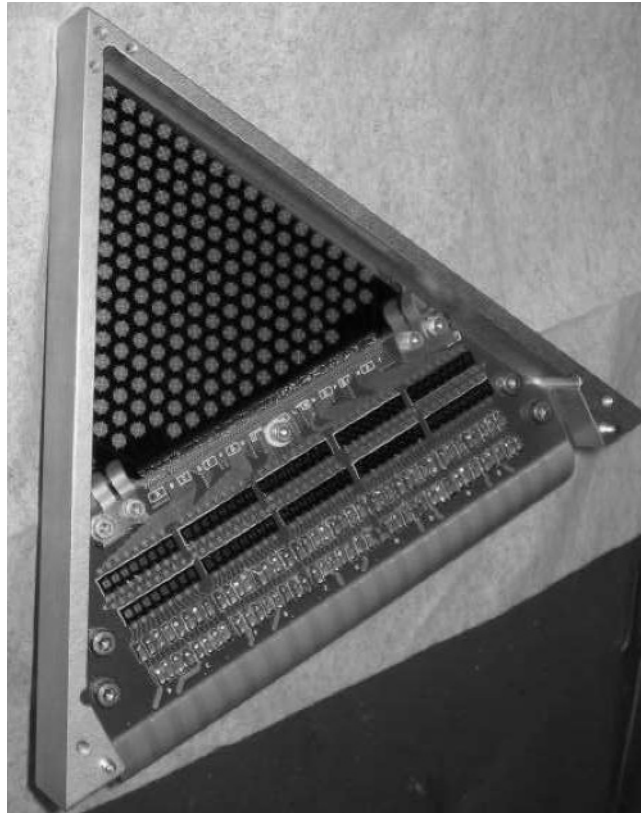


Fig. 10.— 161 element bolometer array (without feedhorns and filters). The spacing between bolometers is ~ 5 mm. Bias filters for the frequency multiplexed readout are on the circuit board at the bottom of the picture.

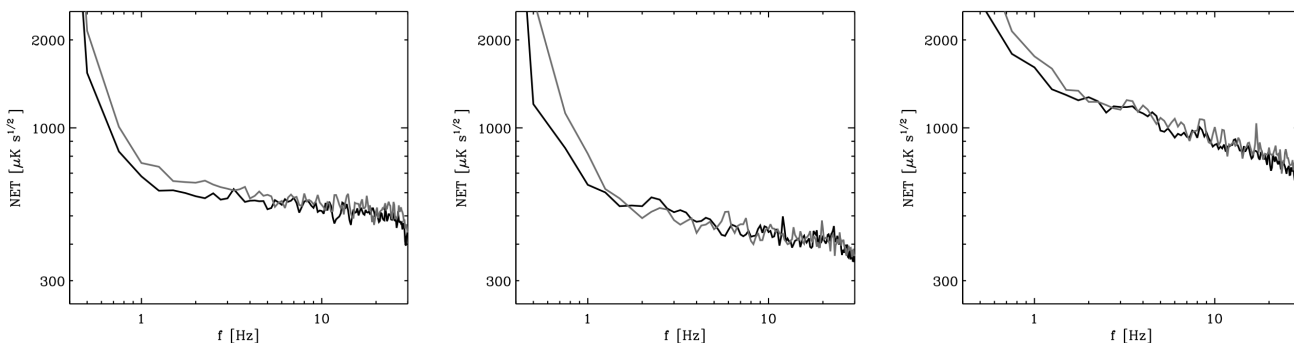


Fig. 11.— NET as a function of frequency for a typical bolometer at $\lambda = 3$ mm (*left panel*), 2 mm (*center panel*), and 1.3 mm (*right panel*). In each plot, the black trace shows data taken while the telescope was stationary, while the gray trace shows data taken while the telescope was scanning at ~ 0.25 degrees/s.

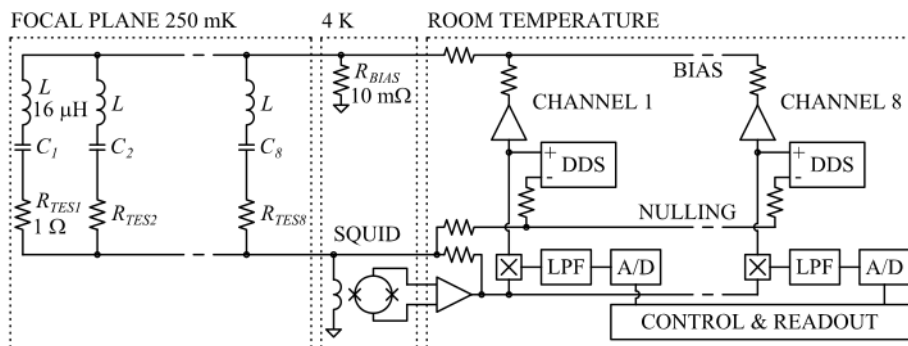


Fig. 12.— Frequency multiplexed SQUID readout. DDS is a direct digital synthesizer, x is a square-wave mixer, LPF is a low-pass, anti-aliasing filter and A/D is a digitizer. Nulling suppresses the bias carriers to reduce the dynamic range at the SQUID input.

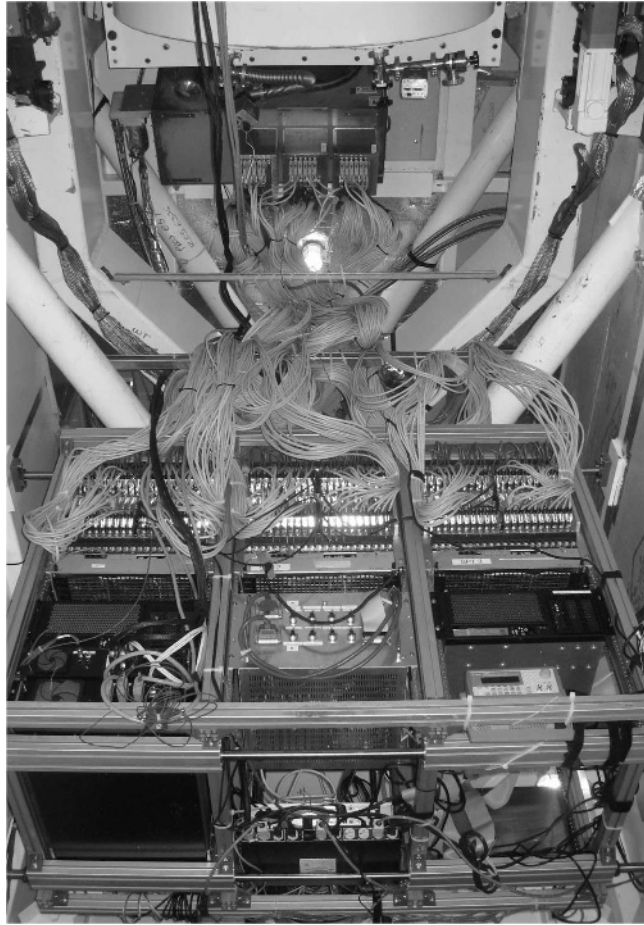


Fig. 13.— Readout electronics. The receiver and optics cryostats are at the top of the picture and the 3 VME crates of bias and demodulator electronics are at the top of the rack. The 2 white tubes immediately above the rack are part of the L frame.

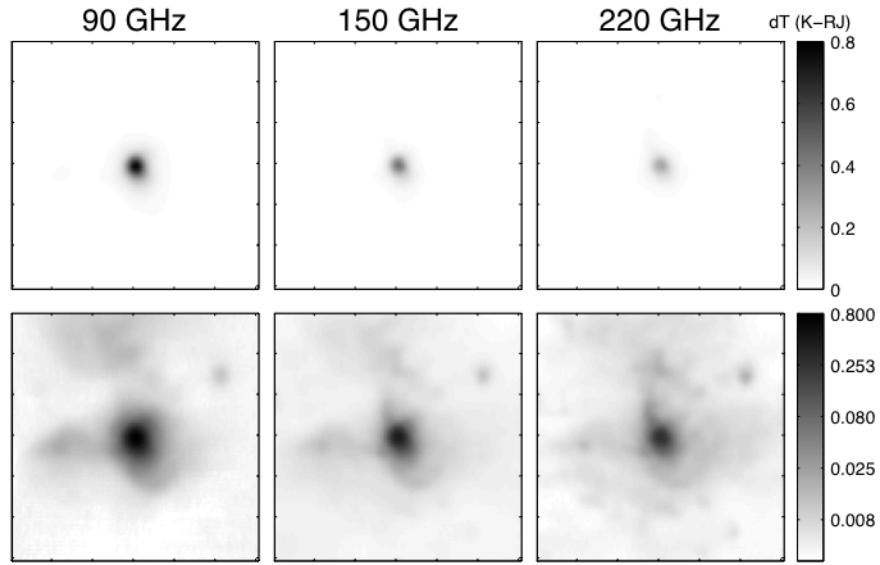


Fig. 14.— SPT images of the galactic HII region RCW38. The top row shows a linear scale and the bottom row shows a logarithmic scale. The extent of each image is $30' \times 30'$. Each image is centered on R.A. $8^h 59^m 06^s$, Decl. $-47^\circ 30' 38''$. Increasing R.A. is to the left and increasing Decl. is up.